Acta Astronautica 203 (2023) 296–307

Contents lists available at ScienceDirect

Acta Astronautica

journal homepage: www.elsevier.com/locate/actaastro

Research Paper

Coupled finite element-discrete element method (FEM/DEM) for modelling hypervelocity impacts

R.M. Færgestad [a,b,*], J.K. Holmen [a,c], T. Berstad [a,b], T. Cardone [d], K.A. Ford [e], T. Børvik [a,b]

[a] Structural Impact Laboratory (SIMLab), Department of Structural Engineering, NTNU – Norwegian University of Science and Technology, Richard Birkelands veg 1a, 7034 Trondheim, Norway
[b] Centre for Advanced Structural Analysis (SFI CASA), NTNU, Richard Birkelands veg 1a, 7034 Trondheim, Norway
[c] Enodo AS, Richard Birkelands veg 1a, 7034 Trondheim, Norway
[d] European Space Agency (ESA), ESTEC, Keplerlaan 1, 2201 AZ Noordwijk, The Netherlands
[e] National Aeronautics and Space Administration (NASA), Johnson Space Center, 2101 E NASA Pkwy, Houston, TX 77058, USA

ARTICLE INFO

Keywords:
Hypervelocity impact
Debris cloud
Whipple shield
FEM to DEM conversion
LS-DYNA

ABSTRACT

Hypervelocity impacts (HVIs) from orbital debris are an increasing threat to current and future missions in low Earth orbit, making spacecraft shielding vital for future space exploration efforts. A debris shield is a sacrificial plate that shatters an impactor into a cloud of particles, distributing the momentum of the impactor over a large area, thus preventing it from perforating the spacecraft. In this study, HVIs on debris shields were modelled in LS-DYNA using a coupled finite element-discrete element method (FEM/DEM), where failed solid elements are converted into discrete particles. The results are compared to experimental data with systematic variation of test configurations from literature for validation. Normal impacts by projectiles with diameters below 1 cm and impact velocities of 6.7 km/s were simulated to study the formation of debris clouds after perforation of a thin plate. Material data for aluminium alloy AA6061-T6 was used in both the target and the projectile. The FEM/DEM method was able to predict the shape of the debris cloud as a function of shield thickness, and a parametric study was performed to investigate the sensitivity of key model parameters. Ballistic limit curves were then determined for velocities from 1 to 14 km/s for a dual-wall Whipple shield and a corresponding monolithic configuration of equal areal mass. Again, the predictions from the FEM/DEM method were close to the results from literature.

1. Introduction

Providing efficient spacecraft shielding and protection from hypervelocity impacts (HVIs) caused by space debris is essential to ensure safe and successful operations of spacecraft and satellites. The development of low-weight effective shields has reduced the risk of critical damage to spacecraft while also minimising the weight and volume of the design. Whipple [1] first introduced the idea of an outer sacrificial shield for spacecraft in 1947. Such Whipple shields consist of a single bumper plate, followed by a rear wall (representing the wall of the spacecraft) at a given standoff distance. The function of the bumper plate, or sacrificial shield, is to break the impacting particle into a cloud of solid, molten and vaporised material that expands in the space behind the bumper. The momentum and energy of the particles are then distributed over a wide area of the rear wall. The rear wall must be thick enough to withstand the blast-like loading from the debris cloud and any solid fragments remaining. The Whipple shield is more mass-effective than a single-wall shield at withstanding a HVI, but it adds additional volume to the design. Experimental HVI tests are expensive and can only be conducted at a few laboratories worldwide. Reliable and versatile numerical models are therefore important to save cost and reduce the number of experimental tests needed when developing debris shielding.

The capability of a shield to protect from projectiles impacting at hypervelocity is described by a ballistic limit equation (BLE). BLEs describe the critical projectile diameter D_C that causes shield failure, typically as a function of impact velocity, impact angle, density, and the shape of the projectile [2]. Failure of the shield is achieved for projectile diameters greater than the critical diameter and is defined as either complete perforation or detached spall from the rear wall. BLEs are typically empirically fitted models made to describe complex phenomena using relatively simple equations.

* Corresponding author at: Structural Impact Laboratory (SIMLab), Department of Structural Engineering, NTNU – Norwegian University of Science and Technology, Richard Birkelands veg 1a, 7034 Trondheim, Norway.
E-mail address: rannveig.m.fargestad@ntnu.no (R.M. Færgestad).

https://doi.org/10.1016/j.actaastro.2022.11.026
Received 18 May 2022; Received in revised form 28 October 2022; Accepted 13 November 2022
Available online 24 November 2022

Several numerical approaches are available when modelling HVIs. Smoothed particle hydrodynamics (SPH) is widely used (e.g. [3–6]) because the meshless formulation allows for straightforward handling of the localised, hydrodynamic material behaviour found under such conditions. SPH is therefore suitable for problems where the medium moves like a liquid. The material is represented by a set of particles that interact with neighbouring particles within a range determined by a smoothing function [7]. Another computational approach that can be applied to HVI problems is the discrete element method (DEM). In DEM models, the material is represented by a collection of independent rigid spheres (particles) interacting at the boundaries, where particles can interact with cohesive and repulsive forces. DEM can either be modelled as dry particles, where a mass–spring–damper system determines the interaction forces between particles, or as wet particles, where capillary forces are accounted for. DEM is most commonly used to model granular materials, but has been applied to HVI with good results, e.g. by Watson and Steinhauser [8]. HVI problems involve different failure modes depending on the velocity and dimensions of the impact configuration. For lower velocities and/or thin targets, fragmentation is the major failure mode. As the velocity and/or target thickness increases, melting and vaporisation become increasingly important. Different modelling approaches may therefore be beneficial for different impact scenarios.

Coupled methods aim to combine the benefits of using particles (SPH or DEM) to describe the localised large deformation behaviour in the impact zone, with the benefit of using the finite elements method (FEM) for the global structural response, by converting distorted finite elements to particles once a criterion is reached. Coupled methods can therefore distinguish between solid and fragmented/melted/vaporised material during HVI, which is not straightforward with a pure SPH or DEM approach.

A number of coupled methods between finite elements and particles have been proposed. Fahrenthold and Horban [9,10] developed a hybrid particle-finite element modelling approach, where particles were used to model contact and volumetric deformation while finite elements represented interparticle tension forces and elastic–plastic deviatoric deformation, showing reasonable agreement with experiments. Johnson [11] presented a method for converting highly strained elements to SPH nodes using a plastic strain criterion. Similarly, Johnson and Stryk [12] used a generalised particle algorithm to represent the meshless particles in their algorithm to convert distorted elements into particles using a plastic strain criterion. More recent works by Johnson et al. [13,14], building on the work of Fahrenthold and Horban [9,10], present combined and hybrid particle-finite element algorithms where both finite elements and meshless particles represent the same material simultaneously, showing good results for high-velocity impact applications. Another coupled approach is finite element reconstruction (FER), where finite elements are reconstructed from SPH particles in the debris cloud [15]. Finally, He et al. [16] applied a coupled FEM/SPH model in LS-DYNA to model the debris cloud in HVI, and found good agreement between the numerical and experimental results.

The main difference between the coupled FEM/SPH and FEM/DEM methods is the definition and governing equations of the particles and how they interact with other particles and parts. In a FEM-SPH approach, the particles will interact with its neighbouring particles within a defined range, while in the FEM-DEM approach, the particles are independent and only interact with other particles and parts if there is contact.

A non-linear Mie–Grüneisen equation of state (EOS) is typically used in HVI modelling since it gives a suitable theoretical description of the pressure states in a shocked solid. However, the influence of the EOS in numerical models was investigated for ballistic impacts with bullets at velocities up to 7 km/s by Børvik et al. [17], showing only minor differences between a linear and non-linear EOS. The linear EOS, relating the pressure linearly to the volumetric strain using the bulk modulus, has the significant benefit that it does not require additional calibration, in contrast to the often complex calibration procedure behind the non-linear Mie–Grüneisen EOS.

Table 1
Configurations in target thickness study. The time of X-ray exposures are given in μs (±0.1 μs), with respect to impact ($\tau = 0$) [18].

Shot ID	t	D	t/D	Velocity	Time [μs]		
	[mm]	[mm]	[–]	[km/s]	τ_1	τ_2	τ_3
4-1395	0.246	9.53	0.026	6.70	−3.4	6.9	19.9
4-1360	0.465	9.53	0.049	6.62	−4.2	7.2	20.3
4-1359	0.592	9.53	0.062	6.78	−3.2	8.2	21.3
4-1289	0.800	9.53	0.084	6.68	−3.4	6.9	19.9
4-1283	0.968	9.53	0.102	6.72	−3.1	7.3	20.4
4-1291	1.549	9.53	0.163	6.71	−3.1	7.2	20.3
4-1352	2.225	9.53	0.234	6.64	−3.5	6.6	20.9
4-1353	4.039	9.53	0.424	6.68	−1.7	8.4	22.6

In this study, a coupled FEM/DEM method in LS-DYNA is applied to simulate HVI by aluminium projectiles on aluminium targets. The numerical results are compared to the experimental studies by Piekutowski [18], where projectiles with 9.53 mm diameter impact targets with thickness 0.246–4.039 mm at 6.7 km/s. Furthermore, the FEM/DEM method is applied to a dual-wall Whipple shield and a monolithic shield of corresponding mass at velocities from 1 to 14 km/s to determine the ballistic limit of the shields. Aluminium projectiles of these sizes and velocities are relevant for the orbital debris found in low Earth orbit, and aluminium is commonly used as the outer bumper in Whipple shields, for example on the International Space Station (ISS) [2]. The work presented in this article evaluates the FEM/DEM method's suitability for HVI applications with aluminium, and forms a basis for further studies investigating more advanced shielding materials with the proposed method.

2. Piekutowski experiments

The numerical results presented in this study were compared to the experimental data by Piekutowski [18], where the formation and description of debris clouds by HVI were investigated. The test configurations in the study were systematically varied with respect to key parameters, making the experimental data set suitable for validating numerical methods against a range of different impact scenarios and failure modes. This paper will focus on the target thickness study, a thorough evaluation of the effects of target-thickness-to-projectile-diameter ratio (t/D) on the debris cloud formation process. Piekutowski used aluminium AA2017-T4 spheres as projectiles and aluminium AA6061-T6 sheets as target plates in the target thickness study. The impact velocity and the projectile diameter (D) were kept constant at 6.7 km/s and 9.53 mm, respectively, while the target thickness (t) was varied from 0.246 to 4.039 mm. Radiographs from an impact test with $t = 0.968$ ($t/D = 0.102$) are shown in Fig. 1. As the t/D ratio was increased at constant impact velocity, a significant expansion of the debris cloud was found, while the size of the fragments at the centre of the debris cloud decreased.

The radiographs in Fig. 1 show the debris cloud at three points in time; the first around $\tau_1 = 3$ μs before the impact, the second around $\tau_2 = 7$ μs after the impact and the third around $\tau_3 = 20$ μs after the impact.

The dimensions, velocities and time of X-ray exposures for all configurations in the target thickness study are presented in Table 1.

Piekutowski's experimental study includes some tests where the aluminium alloy in the target and projectile was varied. Subtle changes in debris cloud properties were found when the projectile was changed from AA2017-T4 to AA1100-O, namely an increase in the number of fragments and a faster radial expansion. The use of AA1100-O and AA2024-T3 targets instead of AA6061-T6 did not measurably affect the debris cloud shape or characteristics.

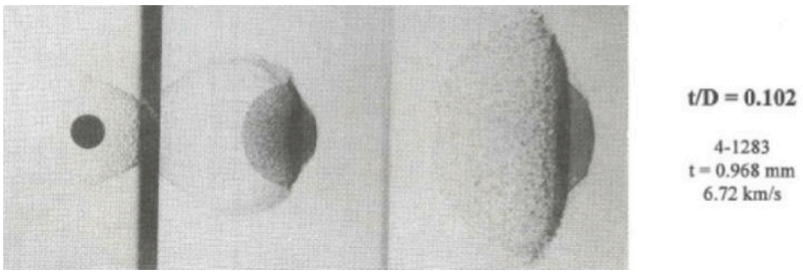

Fig. 1. Radiographs from target thickness study, with t/D = 0.102 at 6.72 km/s impact velocity, shown as a composite image of the impact from three points in time [18].

3. Material modelling

In finite element codes, the stress tensor describing the material state is divided into deviatoric and hydrostatic parts. The deviatoric part is related to the shear strength of the material and is for metals usually described by a pressure-independent constitutive relation. The hydrostatic part relates the pressure, volume and internal energy of the material and is described by an EOS. A majority of the models describing material behaviour under impact and shock conditions are highly non-linear and require complex calibration procedures. This study therefore aims to apply and investigate the simplest modelling approaches available, where the number of calibration steps are minimised and where the model can be extended to new materials with relative ease. The following section presents the constitutive relation, EOS, failure criteria and calibrated material parameters applied in this study.

3.1. Constitutive relation

The constitutive relation applied to HVI on aluminium alloys must account for large plastic strains, high strain rates and thermal softening. Two commonly used models are the Johnson–Cook (JC) model [19] and Steinberg–Guinan (SG) model [20]. In this study, a modified version of the Johnson–Cook (MJC) constitutive relation [21] is used in the numerical simulations, because of its simple calibration procedure and range of validity from low to high strain rates. The equivalent stress in the MJC model is a function of the flow stress, the strain rate and the temperature, and is expressed as

$$\sigma_{\mathrm{eq}} = \left(\sigma_0 + \left[\sum_{i=1}^{2} Q_i(1-\exp(-C_i p))\right]\right)\left(1+\frac{\dot{p}}{\dot{p}_0}\right)^{c}\left(1-\left[\frac{T-T_0}{T_{\mathrm{m}}-T_0}\right]^{m}\right) \tag{1}$$

where σ_0 is the yield stress, Q_i and C_i are hardening parameters, p and $\dot{p}$ are the equivalent plastic strain and strain rate, respectively, $\dot{p}_0$ is a user-defined reference strain rate and c governs the strain rate sensitivity of the material. T is the temperature, T_0 is a reference temperature, T_{m} is the melting temperature, and m governs the thermal softening of the material. Under the assumption of adiabatic conditions, which is reasonable in HVI, the temperature change is defined as

$$\Delta T = \int_0^p \chi \frac{\sigma_{\mathrm{eq}} \mathrm{d}p}{\rho C_{\mathrm{p}}} \tag{2}$$

where χ is the Taylor–Quinney empirical coefficient, ρ is the material density, and C_{p} is the specific heat capacity.

The material parameters for the MJC constitutive model can be determined from uniaxial tension tests conducted at strain rates and temperatures suitable for the application at hand.

3.2. Equations of state

An EOS relates the pressure, volume, and internal energy of matter, and describes the hydrostatic behaviour of the material. A linear EOS is generally used for applications at low pressures (<20 GPa), while a non-linear EOS is considered suitable for applications at high pressures (>20 GPa).

3.2.1. Linear EOS

For low velocities and pressures, the EOS relates the pressure to the volumetric strain linearly using the bulk modulus, and is given as

$$P(\varepsilon_{\mathrm{v}}) = -K\varepsilon_{\mathrm{v}} = -\frac{E}{3(1-2\nu)}\varepsilon_{\mathrm{v}} \tag{3}$$

where P is the pressure, K is the bulk modulus and ε_{v} is the volumetric strain. The linear EOS can therefore be determined for a given material using only the two elastic material parameters E and ν.

3.2.2. Non-linear EOS

For higher velocities and pressures, the effect of internal energy can be significant, and the relationship between pressure and volume may become non-linear. The Mie–Grüneisen EOS is valid for inert solids and is widely used to describe pressure states in shocked solids [22]. The Mie–Grüneisen EOS can be expressed as

$$P(\rho,e) = P_0(1-\Gamma\eta) + \frac{\rho_0 c_0^2 \eta}{1-s\eta}\left(1-\frac{\Gamma\eta}{2}\right) + \Gamma\rho_0(e-e_0) \tag{4}$$

where P is the pressure, ρ is the density, e is the internal energy, Γ is the Grüneisen gamma, $\eta = 1-\rho_0/\rho$, c_0 is the elastic wave speed, and s is the linear Hugoniot slope coefficient. Γ and s must be calibrated for a given material through for example flyer-plate impact tests. Alternative formulations of the Mie–Grüneisen EOS also use an additional parameter, a, i.e., the first-order volume correction to the Grüneisen gamma [23].

3.3. Failure criteria

In this study, failure can occur either when the element temperature reaches a critical temperature or when the Cockcroft–Latham (CL) fracture criterion [24] is reached. The critical temperature T_{c} is set as 0.9 times the melting temperature T_{m}. The temperature criterion does not distinguish between molten and vaporised material, but if a distinction is needed it can be estimated based on the materials and impact conditions at hand. The CL fracture criterion is an uncoupled phenomenological ductile fracture criterion depending on the plastic strain as well as the stress triaxiality ratio σ^* and the Lode parameter L through the maximum principal stress σ_{I}. The damage variable is given by

$$\begin{aligned}\omega &= \frac{1}{W_{\mathrm{C}}}\int_0^p \max(\sigma_{\mathrm{I}},0)\,\mathrm{d}p \\ &= \frac{1}{W_{\mathrm{C}}}\int_0^p \max\left(\sigma^* + \frac{3-L}{3\sqrt{3+L^2}},0\right)\sigma_{\mathrm{eq}}\,\mathrm{d}p\end{aligned} \tag{5}$$

Fracture occurs when the damage $\omega = 1$. High levels of stress triaxiality give a faster damage evolution. Generalised tension ($L=-1$) gives a faster damage evolution, generalised compression ($L=+1$) gives a slower damage evolution, with generalised shear ($L=0$) in between. When using the CL criterion in combination with the MJC constitutive model, σ_{eq} depends on the strain rate and temperature, and the failure strain increases with T and decreases with $\dot{p}$. The CL criterion is therefore able to qualitatively represent variation in ductility with stress state, strain rate and temperature. The fracture parameter W_{C} is constant, and can be determined from a single uniaxial tensile test as long as local strain measurements are carried out [25].

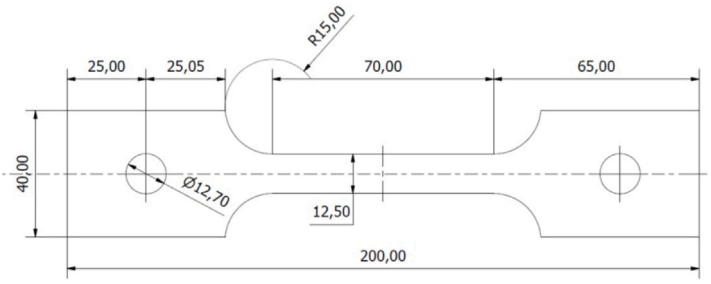

Fig. 2. Dimensions of tensile test specimen with 2 mm thickness.

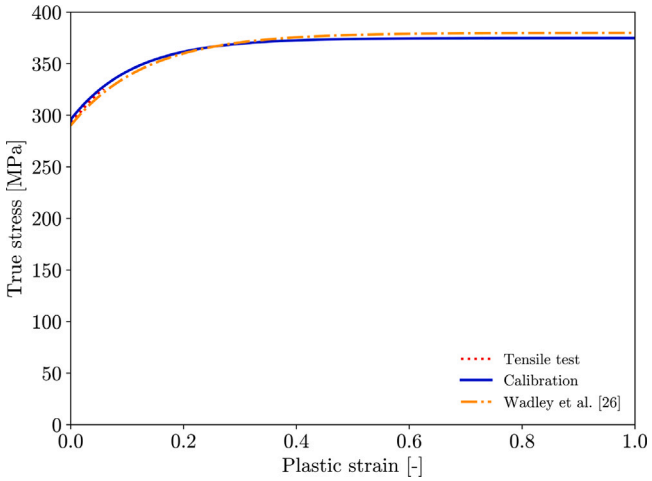

Fig. 3. Hardening parameters for AA6061-T6 calibrated to the stress–strain curve obtained from the tensile test. Extrapolated calibration is compared to calibration by Wadley et al. [26].

3.4. Material parameters

To simplify the material modelling, material data for AA6061-T6 was used for both the projectile and the target. Piekutowski [18] conducted tests where the aluminium alloys in the projectile and target were varied, without observing any significant effect on the structural response. Based on these results this simplification is deemed reasonable for this study. The material parameters for the constitutive relation were calibrated by performing uniaxial quasi-static tensile tests, with specimen geometry as shown in Fig. 2. Two-dimensional digital image correlation (2D-DIC) analysis was used to measure the engineering strain during the test, which was combined with force measurements from the testing machine to produce an engineering stress–strain curve. Based on the engineering stress–strain curve, the true stress–plastic strain curve until necking was extracted. The hardening parameters were determined by curve fitting to this curve, and extrapolated to a plastic strain of 1.0, as shown in Fig. 3. The calibrated hardening parameters were compared to the calibration by Wadley et al. [26], and were found to give similar results. A common alternative to the direct calibration procedure presented above is to inverse model the material test as done in e.g. Granum et al. [27], which gives material data all the way to fracture.

Table 2 presents the hardening parameters for the MJC constitutive model, calibrated from the tensile test, and the fracture parameter W_C for the CL fracture criterion, as calibrated by Wadley et al. [26]. The applied material model is similar to material model 107 (*MAT_MODIFIED_JOHNSON_COOK) in LS-DYNA, based on the work by Børvik et al. [21]. However, material model 107 cannot be combined with a non-linear EOS, so in this study a user-defined material subroutine (UMAT) was implemented to combine the MJC model with the non-linear Mie–Grüneisen EOS.

Table 2
Calibrated parameters for the modified Johnson–Cook constitutive model and the Cockroft–Latham fracture criterion.

σ_0 [MPa]	Q_1 [MPa]	C_1 [–]	Q_2 [MPa]	C_2 [–]	W_C [MPa]
292.6	2.7	2160.7	79.1	8.94	278

Table 3
Mie–Grüneisen EOS material parameters for AA6061-T6 [28].

s [–]	Γ [–]	a [–]	c_0 [m/s]
1.40	1.97	0.48	5240

Table 4
Material parameters for AA6061-T6.

ρ [$\frac{kg}{m^3}$]	E [GPa]	ν [–]	c_p [$\frac{J}{kg\ K}$]	χ [–]	T_0 [K]	T_c [K]	T_m [K]	C [–]	m [–]	α [K^{-1}]
2700	70	0.33	910	0.9	293	804	893	0.001	1	$2.34 \cdot 10^{-5}$

Table 3 presents the material parameters for the non-linear Mie–Grüneisen EOS with AA6061-T6, taken from Steinberg [28] and applied in LS-DYNA using the keyword *EOS_GRUNEISEN. Additional material parameters required in the material model for AA6061-T6 are adapted from the literature as standard values for 6000-series of aluminium alloys and are presented in Table 4.

4. Numerical modelling and setup

The simulations in this study were conducted using LS-DYNA [29] (version R12.0.0). The simulations were run utilising 16 cores of a computer cluster node (Intel Xeon X5680). The computational times ranged from 40 min to 22 h, depending on the problem at hand. Numerical models were established to (1) reproduce the Piekutowski experimental target thickness study, and (2) to obtain ballistic limit curves for monolithic and dual-wall Whipple shields.

When using the coupled FEM/DEM method in LS-DYNA, the target and projectile parts are initially modelled with 3D solid elements. The conversion from solid elements to discrete element spheres (DES), i.e., particles, is achieved through the keyword *DEFINE_ADAPTIVE_SOLID_TO_DES. The keyword adaptively transforms a Lagrangian solid part or part set to particles when the Lagrangian solid elements comprising those parts fail. One (or more if desired) particles will be generated for each failed element as debris. The particles replacing the failed element inherit the properties of the element, including mass and kinematical state [30]. The particles have limited contact with each other since the debris cloud radially expands, and the contact parameters between particles are therefore assumed to have low importance. A static and dynamic friction coefficient $\mu = 0.01$ was applied for nodes-to-surface and single surface eroding contact. The coefficient values are inherently difficult to verify experimentally, and will be investigated numerically in the parametric study presented in Section 5.3.

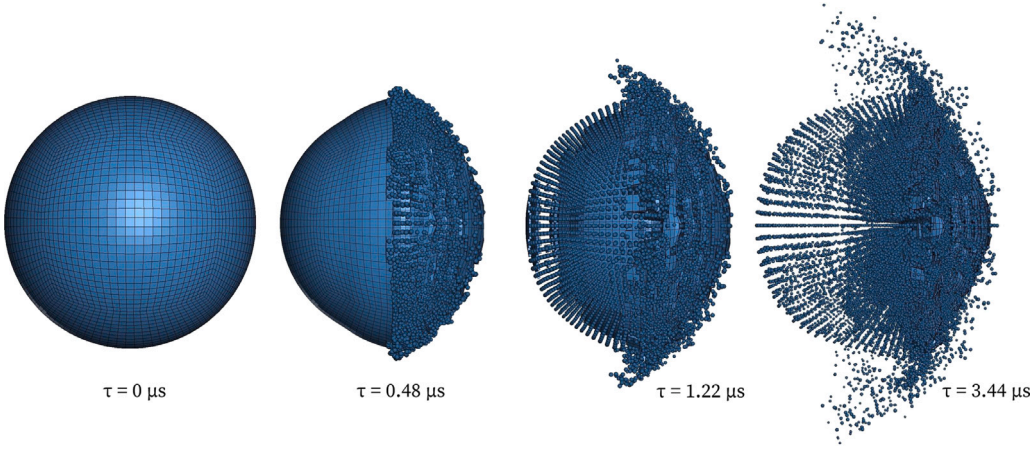

Fig. 4. Conversion from solid elements to particles after impact, shown for t/D = 0.084 at 6.7 km/s impact velocity.

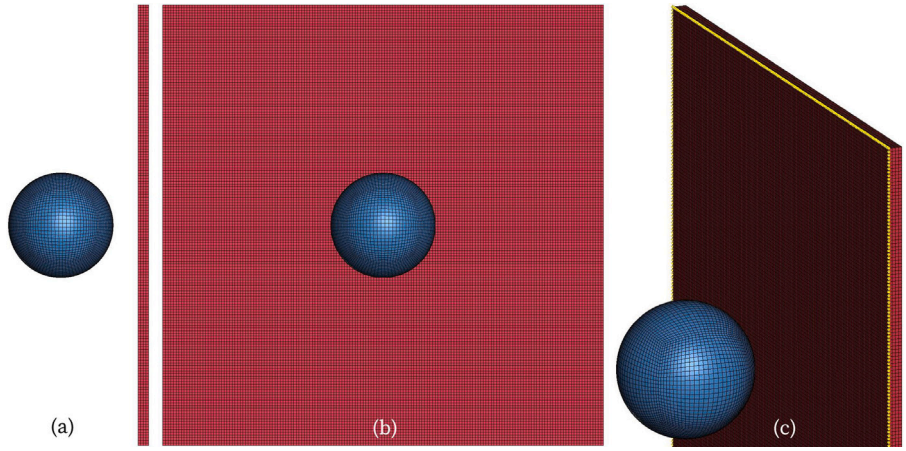

Fig. 5. Finite element model of Piekutowski configuration with t/D = 0.102, shown from the (a) side, (b) front and (c) with highlighted boundary condition.

In this study, failure of an element occurs when the CL fracture criterion is fulfilled, or when the temperature of an element exceeds the critical value. The first criterion that is fulfilled for an element is counted as the mode of failure. Fig. 4 illustrates a typical conversion process following an impact.

For aluminium-on-aluminium impacts, the impact velocity must be above 10 km/s to equal or exceed the vaporisation temperature of aluminium [31]. For the Piekutowski studies at 6.7 km/s it is therefore assumed that fragmentation and melting are the two main failure modes, and the converted particles then represent small solid fragments and/or droplets of molten material. For the Whipple studies, with impact velocity ranging from 1 to 14 km/s, vaporisation may be a failure mode above 10 km/s, and the converted particles in this regime represent mainly molten and vaporised material.

The element size in the numerical models was required to be small enough to accurately capture the material response, but large enough to keep the computational time as low as possible. A preliminary mesh sensitivity study found that the results converged when the element size was around 0.3 mm.

4.1. Piekutowski configurations

The finite element model of the Piekutowski configuration with t/D = 0.102 is shown in Fig. 5 with side and front views, and with boundary conditions highlighted.

The targets in the experimental studies of Piekutowski were modelled with an element size of approximately 0.25 mm for all configurations, and the number of elements over the target thickness increased in accordance with the increased t/D ratio. The number of elements in the target ranged from 26 569 with t/D = 0.026 to 399 424 with t/D = 0.424. The element size in the projectile with a diameter of 9.53 mm varied from 0.1 mm in the centre to 0.35 mm in the outer layer, due to the non-uniform mesh structure of spheres in LS-DYNA, leading to a total of 137 781 elements. Boundary conditions restricting nodal translation in the impacting direction were added to the front-facing outer edge of the targets to recreate the boundary conditions from the Piekutowski experiments.

4.2. Whipple shield configurations

The Whipple shield setup used in the numerical analysis corresponds to the BLE curve presented by Christiansen [31], and the geometry of the monolithic and Whipple shields are presented in Fig. 6.

The setup of the dual-wall Whipple shield was similar to the Piekutowski configurations, only with an added rear wall representing the spacecraft. Boundary conditions restricting translation in the impacting direction were added to the bumper and rear wall along the front-facing outer edges of the walls. Width and length were set to 20 mm for the bumper and 60 mm for the rear wall. An element size of approximately 0.25 mm was used for both walls, giving a total of 34 445 elements in the bumper and 773 968 elements in the rear wall. An increased width and length of 90 mm was used for the rear wall when the impact velocity was >5 km/s, in order for the rear wall to be larger than the debris cloud diameter. This larger rear wall had an element size of approximately 0.32 mm and a total of 789 610 elements.

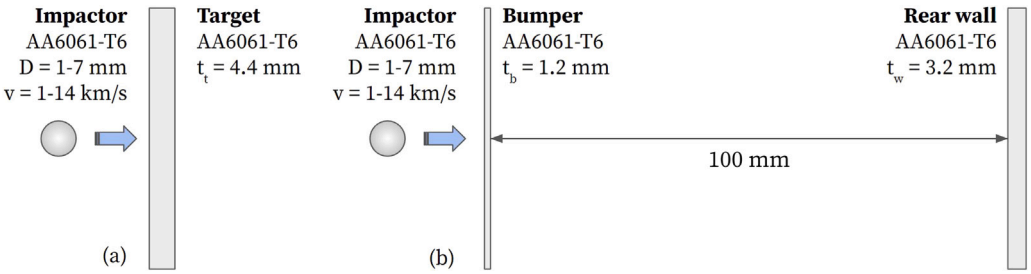

Fig. 6. Geometry of (a) monolithic and (b) Whipple shields.

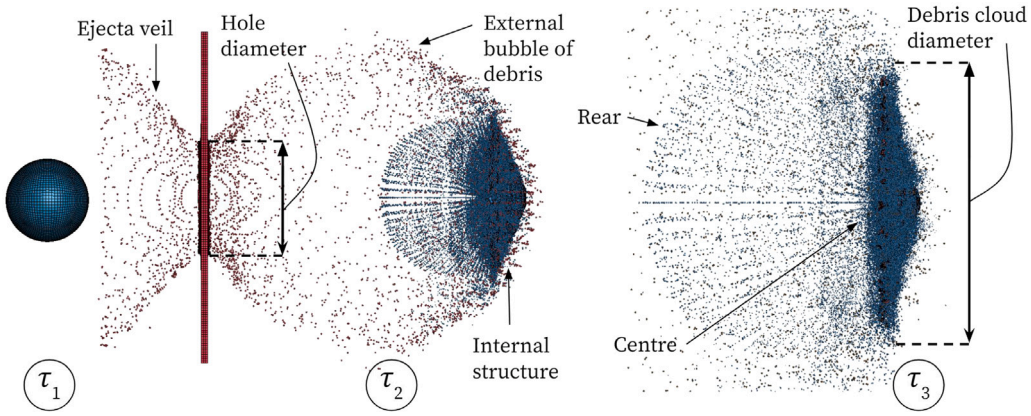

Fig. 7. Measurement points and major elements of the numerical debris cloud, shown for t/D = 0.084 at 6.7 km/s impact velocity.

The setup of the monolithic shield was identical to the Piekutowski configurations, only with a change in the dimensions. The monolithic shield had a thickness of 4.4 mm (equal to the sum of the bumper and rear wall in the Whipple setup), and a width and length of 20 mm. An element size of approximately 0.25 mm gave a total of 108 800 elements in the monolithic shield.

5. Numerical results – formation of debris clouds

The numerical results with the FEM/DEM method applied to Piekutowski's target thickness study are presented below, with a discussion of the method's ability to describe fragmentation and melting, a comparison with Piekutowski's experimental results, and a parametric study to investigate the model sensitivity.

5.1. Features of FEM/DEM debris clouds

The numerical results are compared to the experimental results by visual inspection and measurements of the debris clouds, as illustrated in Fig. 7. The debris cloud diameter, mass and residual velocity are measured at τ_3, corresponding to the experimental configurations presented in Section 2. The debris cloud diameter in the experimental results is measured as the diameter of the centre disc, and is not measured for t/D = 0.163, 0.234 and 0.424, since these did not produce distinct disc diameters. The residual velocity in the experimental results is calculated as the average residual velocity of the centre disc in the debris cloud, where the majority of the projectile mass is located, and in the numerical simulations it is measured at the centre of mass of the projectile. The percentage of solid elements in the projectile converted to particles is calculated by comparing the mass of the projectile solid elements at τ_1 and τ_3.

Fig. 8 (t/D = 0.084) shows the composition of the debris cloud, where the target particles make up the external bubble of debris and the projectile particles and solid elements make up the internal structure. The internal structure consists of a spherical rear element and a disc-shaped centre element where the centre of mass of the cloud is typically located. The debris cloud is shown from the rear side of the target in Fig. 9, showing the radial and symmetric distribution of solid elements. One large fragment is found at the centre of the debris cloud.

5.2. Target thickness study

Figs. 10 and 11 show some of the results from the target thickness study. The computational time ranged from 40 min with t/D = 0.026 to 5 h with t/D = 0.424.

There is good agreement by visual inspection between the numerical results and the experimental results for the target thickness study. The linear EOS generally gives a spherical internal structure of the debris cloud, while the non-linear EOS gives an oval internal structure.

In addition to the visual comparison with the experimental results, debris cloud measurements were taken to quantitatively evaluate the numerical results. Table 5 presents the results for some key measurement points in the target thickness study, as presented in Section 5.1, and the experimental results are compared to the numerical results with linear and non-linear EOS. Corresponding plots are shown in Fig. 12.

The debris cloud diameter, shown in Fig. 12a, measures the outer diameter of the disc of projectile particles located at the front of the debris cloud, as illustrated in Fig. 7. The FEM/DEM method produces a debris cloud with a smaller diameter than the experimental results, and simulations applying the linear EOS are closer to the experimental results for most of the t/D ratios. The deviation between the experimental and numerical debris cloud diameter is most likely tied to the FEM/DEM conversion process and parameters, as well as the element size, as this controls how the particles are spread out after the impact. The hole diameter, shown in Fig. 12b, measures the hole in the target after the impact. The hole diameter increases with increasing t/D ratio using both a linear and non-linear EOS, and the results with a linear EOS are closer to the experimental results for t/D below 0.1 and the results with a non-linear EOS are closer for t/D above 0.1. The residual

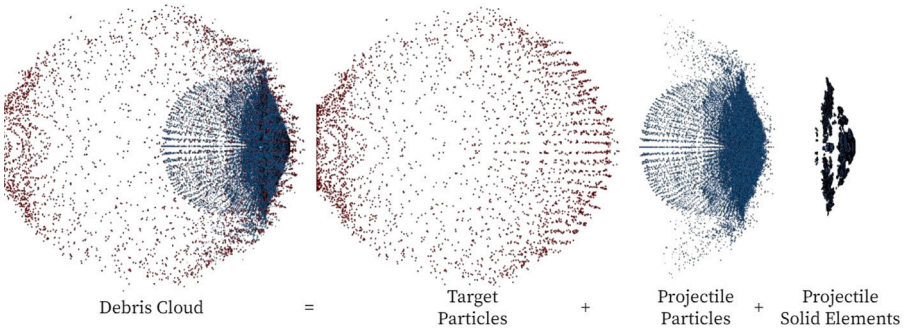

Fig. 8. Components of the numerical debris cloud, shown for $t/D = 0.084$ at 6.7 km/s impact velocity.

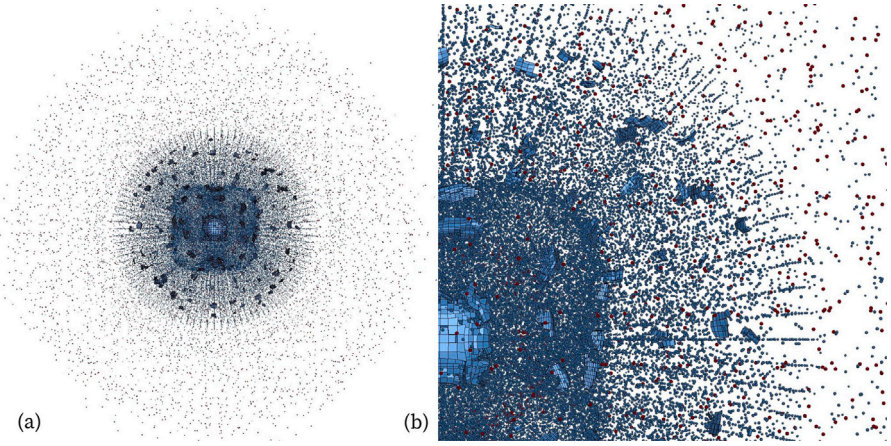

Fig. 9. Full (a) and detailed (b) rear view of debris cloud, shown for $t/D = 0.084$ at 6.7 km/s impact velocity.

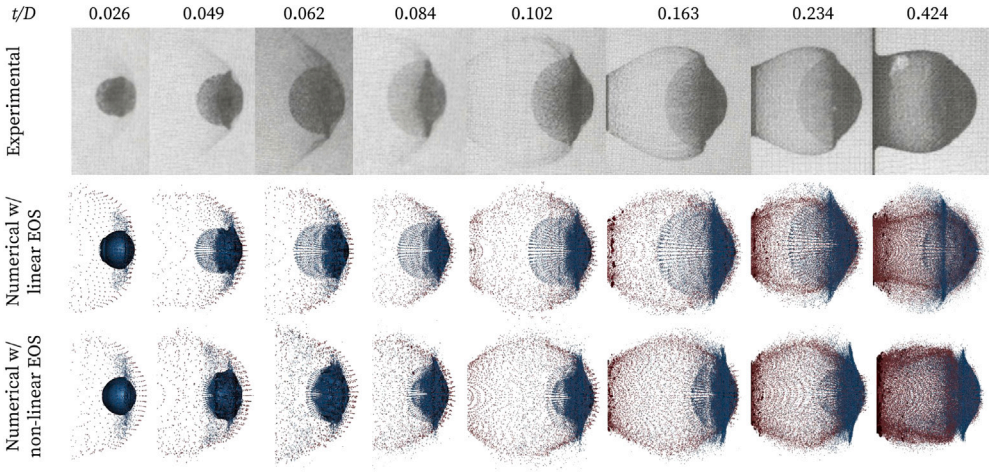

Fig. 10. Numerical results from the target thickness study at $\tau_2 = 7$ μs after impact, with linear and non-linear EOS, compared to Piekutowski's experimental results [18].

velocity of the debris clouds, shown in Fig. 12c, is a useful parameter when comparing the numerical and experimental results, because of the key role it plays in describing the momentum and kinetic energy of the fragments in the cloud and the damage they can inflict on spacecraft. The residual velocity decreases with increasing t/D ratio for simulations using both a linear and non-linear EOS, but the results with a linear EOS are significantly closer to the experimental results than with a non-linear EOS, and the difference increases with increasing t/D ratio.

Fig. 13 shows the percentage of projectile solid elements converted to particles and the percentage of converted particles representing molten material, as a function of the t/D ratio. The percentage of solid material in the debris cloud describes the conversion from solid elements to particles and gives an understanding of the method's ability to describe fragmentation and melting, and distinguish between solid and molten material in the debris cloud. Elements are converted to a discrete particle either due to the CL fracture criterion, or when the element temperature exceeds the critical value. The criterion that is reached first is counted as the cause of failure for the element. Fig. 13a shows that the percentage of solid material in the debris cloud rapidly decreases as the t/D ratio increases, for both linear and non-linear EOS, and more than 95 percent of the projectile has been

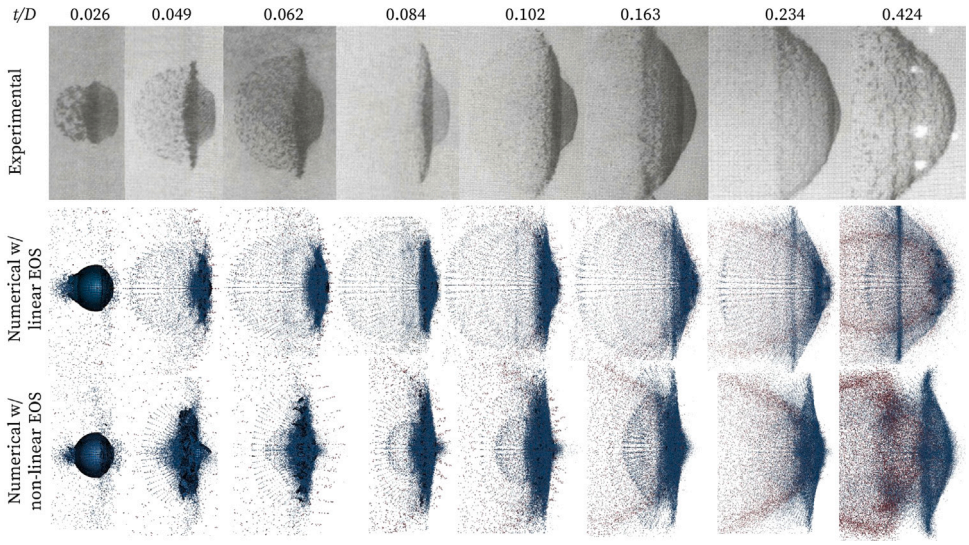

Fig. 11. Numerical results from the target thickness study at $\tau_3 = 20$ μs after impact, with linear and non-linear EOS, compared to Piekutowski's experimental results [18].

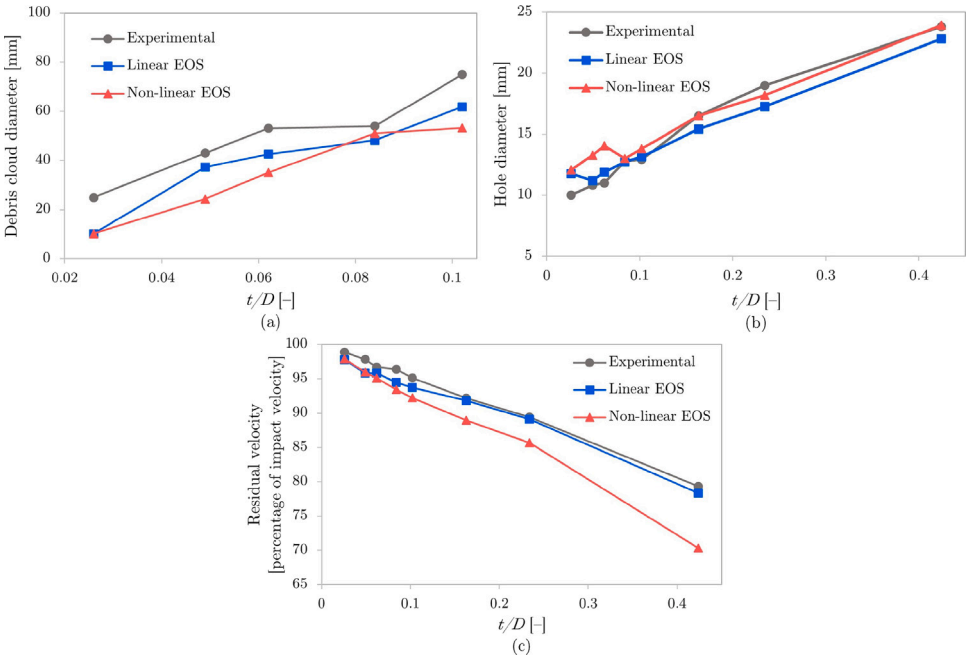

Fig. 12. Measurements of debris clouds as a function of t/D: (a) Debris cloud diameter, (b) Hole diameter, (c) Residual velocity.

converted to particles after the impact for t/D ratios above 0.1. Fig. 13b shows that the percentage of conversion to discrete particles due to temperature increases with increasing t/D ratio, except for with t/D = 0.026, i.e., for the thinnest target. The linear and non-linear EOS show similar patterns, but conversion due to temperature is higher with the non-linear EOS for all t/D ratios.

The regions of the model where elements are converted due to temperature are marked in Fig. 14. Elements are mostly converted due to temperature on the front side of the projectile in the outer element layers. Some elements on the front side of the target are also converted due to temperature. The majority of the conversion due to temperature happens during the initial impact between the projectile and target, where the temperature is highest. As the debris cloud develops after the impact, it then follows that the converted particles at the front of the debris cloud are a combination of fragmented and molten material, while the rear of the debris cloud mainly consists of fragmented material.

5.3. Parametric study

Parametric studies were performed to investigate the sensitivity of the FEM/DEM method to changes in key model parameters. The configuration with t/D = 0.049 and 6.7 km/s impact velocity was selected as a baseline model. Relevant values were selected for each parameter, and simulations were performed for each configuration. The change in percentage of solid elements converted to particles was selected as the response parameter, in order to further study the conversion process from solid elements to particles. The residual velocity of the debris cloud was also investigated as a response parameter, but was found to be insensitive to parameter changes (less than 0.5% change for all

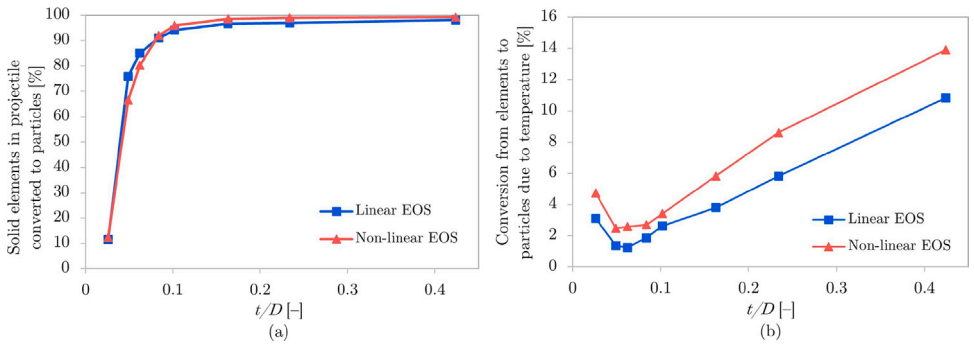

Fig. 13. Measurements of conversion from solid elements to discrete particles as a function of t/D. (a) Percentage of projectile solid elements converted to particles. (b) Percentage of converted particles representing molten material.

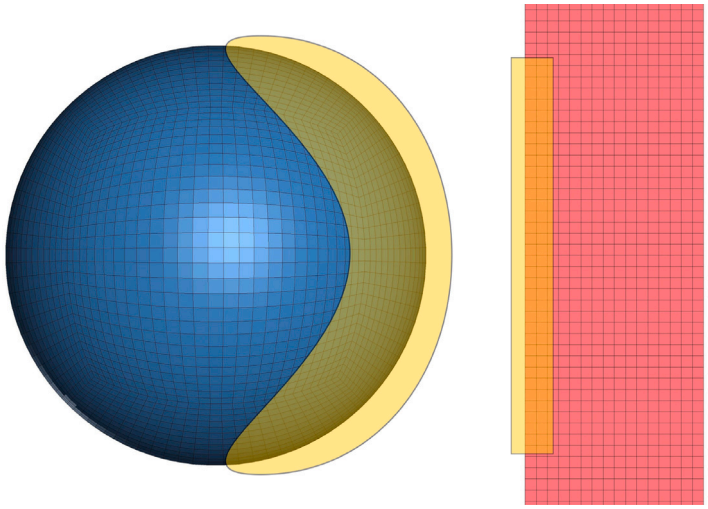

Fig. 14. Regions are marked in yellow where the majority of conversion from elements to particles due to temperature occurs.

Table 5
Quantitative results from target thickness study. Each measured feature from the experimental study [18] (denoted 'Exp' in the table) is compared to the corresponding feature in the numerical simulations with linear and non-linear EOS (denoted 'Lin' and 'Non-lin', respectively, in the table). For t/D = 0.163, 0.234 and 0.424, a distinct cloud diameter could not be measured experimentally.

t/D	Residual velocity [%]			Cloud diameter [mm]			Hole diameter [mm]		
Result	Exp	Lin	Non-lin	Exp	Lin	Non-lin	Exp	Lin	Non-lin
0.026	98.9	97.8	97.9	25	10	10	10.0	11.8	12.1
0.049	97.9	95.8	96.0	43	37	24	10.8	11.2	13.3
0.062	96.7	95.8	95.1	53	43	35	11.0	11.9	14.1
0.084	96.4	94.5	93.4	54	48	51	12.8	12.7	13.0
0.102	95.2	93.7	92.2	75	62	53	12.9	13.1	13.8
0.163	92.2	91.8	89.0	–	–	–	16.5	15.4	16.5
0.234	89.4	89.1	85.7	–	–	–	19.0	17.2	18.2
0.424	79.3	78.4	70.3	–	–	–	23.8	22.8	23.9

Table 6
Parametric study setup, with t/D = 0.049 at 6.7 km/s as baseline model.

Parameter	Baseline model	Value #1	Value #2	Value #3
No. of elements	137 000	28 000	70 000	189 000
EOS [–]	Linear	Non-linear	–	–
Density ρ [kg/m^3]	2700	5400	7800	–
Friction μ [–]	0.01	0	0.05	–
W_C [MPa]	278	100	200	350
Damping coeff. [–]	0.0	0.5	1.0	–

tested parameters), and will therefore not be discussed further in this study. The parameters and values used in the parametric study are presented in Table 6.

The resulting change in percentage of solid elements converted to particles after varying the parameter values according to Table 6 are shown in Fig. 15.

The increase or decrease of converted elements compared to the baseline value shows that the FEM/DEM method is sensitive to some parameters and relatively insensitive to others. The CL fracture parameter W_C is found to be the most influential parameter, and it is found that the percentage of solid elements converted to particles increases as expected with low W_C values and decreases with high W_C values. The density is also found to be an important parameter, and the percentage of solid elements converted to particles increases with high density ρ values. The FEM/DEM method is also sensitive to the EOS, as previously stated, and fewer elements are converted to particles with the non-linear Mie–Grüneisen EOS than with the linear EOS. Further, the parametric study shows that decreasing the number of elements in the model also increases the percentage of solid elements converted to particles, and increasing the number of elements decreases it. The least sensitive parameters in the study were the friction and damping coefficients which gave minor changes in the percentage of solid elements converted to particles.

It should be emphasised that this parametric study only investigates the configuration with t/D = 0.049 at an impact velocity of 6.7 km/s. Configurations with thicker targets, lower velocities and different materials are not expected to exhibit the exact same sensitivities, and should be investigated on their own to draw a stricter conclusion.

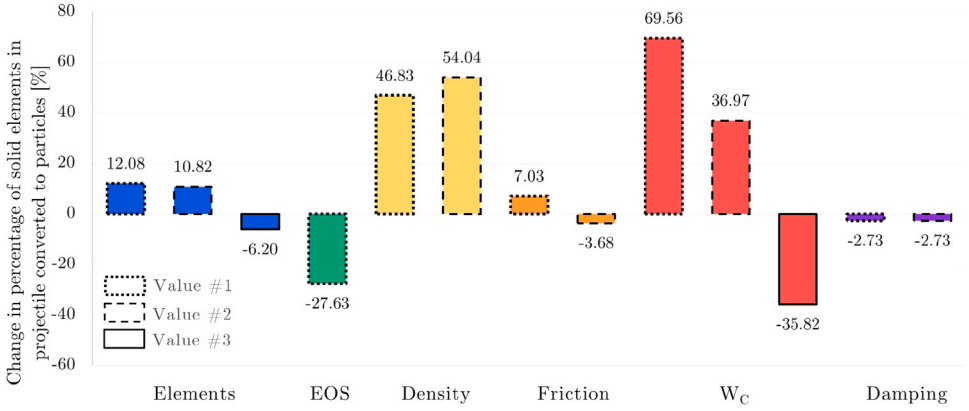

Fig. 15. Parametric study results: Change in percentage of solid elements converted to particles at $\tau_3 = 20$ μs after impact, compared to the baseline model with $t/D = 0.049$ at 6.7 km/s impact velocity.

6. Numerical results – Whipple shields

Simulations of monolithic and dual-wall Whipple shields with the configurations presented in Section 4.2 were performed with impact velocities from 1 to 14 km/s and projectile diameters from 1 to 7 mm, and compared to the empirical BLE curve by Christiansen [31]. The empirical BLE curve is based on experimental test data for impact velocities below 7 km/s, since test data above this velocity was unavailable when the curve was developed. The BLE was extrapolated for impact velocities higher than 7 km/s, giving a conservative result in this regime of the curve.

The resulting numerical ballistic limit curves provide an understanding of the FEM/DEM method's ability to accurately predict the capacity of a given shield configuration. Iterations of projectile diameter were performed at each velocity until the critical diameter was determined. Failure of the shield was defined as perforation or spalling from the rear wall. Because of the long termination time needed to see the full response of the rear wall near the ballistic limit, the computational time was around 10–22 h for the Whipple shields. A linear EOS was applied in all Whipple shield simulations, due to the close match between experimental and numerical residual velocities found in the numerical study of Piekutowski's target thickness study.

The result from a dual-wall Whipple shield impacted by a projectile with a diameter of 3.8 mm at 2 km/s is shown in Fig. 16 at four different times. A large solid fragment is present in the debris cloud at $\tau = 20.2$ μs and $\tau = 60.6$ μs, along with several smaller solid fragments. This corresponds well with the theory of Whipple shields, since the impact velocity in this simulation is below the hydrodynamic transition velocity (roughly estimated to be around 3–4 km/s), transforming the impacting solid into a fluid. Consequently, the mostly intact solid projectile will cause great damage to the rear wall. At $\tau = 90.9$ μs, local deformation can be seen where the large solid fragment impacted, and spalling can be seen from the rear side of the rear wall.

The result from a dual-wall Whipple shield impacted by a projectile with a diameter of 5.2 mm at 8 km/s is shown in Fig. 17 at four points in time. Here, the impact velocity falls within the complete melt regime, and the projectile is expected to be fully converted to particles that impact the rear wall in a similar manner as a blast load, leading to mostly global deformations.

The debris cloud Fig. 17 can be seen fully converted to particles at $\tau = 2.5$ μs and 12.6 μs, with a higher density of particles near the centre of the cloud. The cloud expands radially as it moves across the standoff distance and impacts the rear wall over a wide area, leading to some spalling on the rear side of the rear wall. Global deformation of the rear wall can be seen around the spalling point. The majority of the particles are reflected back towards the bumper.

6.1. Ballistic limit curves for monolithic and Whipple shields

The resulting ballistic limit curves for the monolithic and Whipple shields are shown in Fig. 18, compared to the corresponding empirical ballistic limit curve by Christiansen [31]. These were obtained by marking each simulated combination of projectile diameter and impact velocity as either 'Failure' or 'No failure'. The resulting ballistic limit curves then define the critical projectile diameter that causes failure at each velocity.

The numerical ballistic limit curves for the monolithic and Whipple shields are generally in very good agreement with the empirical curves by Christiansen [31]. The numerical results for the Whipple shield are somewhat non-conservative up to 7 km/s, close to the empirical curve between 7 km/s and 10 km/s, and non-conservative above 10 km/s. The ballistic limit decreases gradually for velocities above 10 km/s with the empirical curve, while the numerical results show no change in the ballistic limit above 10 km/s. The numerical results with the monolithic shield are non-conservative up to 3 km/s, equal to the empirical curve between 3 and 10 km/s and somewhat non-conservative for velocities above 10 km/s.

In general, the results show that the FEM/DEM method is able to determine the capacity of a Whipple shield, with slightly non-conservative results. The reason for the non-conservative result for impact velocities below 7 km/s may be a combination of several factors. The numerical results presented in Section 5 showed that the debris cloud diameter is smaller than in the experimental study. In the Whipple shield configurations, this means that the rear wall is impacted over a smaller area than in corresponding experimental tests, thereby giving a different distribution of mass in the impact. In the velocity regime up to 7 km/s, the failure mode goes from the ballistic regime where the projectile is typically not fractured, to the fragmentation and partial melt regime, where the projectile is increasingly affected by fragmentation and melting as the impact velocity increases. It is therefore reasonable to assume that the parameters controlling the conversion from solid elements to discrete particles are particularly important in this regime. The parametric study in Section 5.3 found that the model is sensitive to the CL fracture parameter W_C, showing a decrease in conversion from solid elements to particles with increased values of W_C. Since larger solid fragments inflict the most damage on the rear wall, the W_C parameter is expected to influence the numerical ballistic curve, and further studies into the calibration and application of the CL fracture criterion in HVI problems are suggested. Additional factors which may have influenced the numerical ballistic curve are the element size and boundary conditions imposed on the shields and the contact and friction forces between elements and particles.

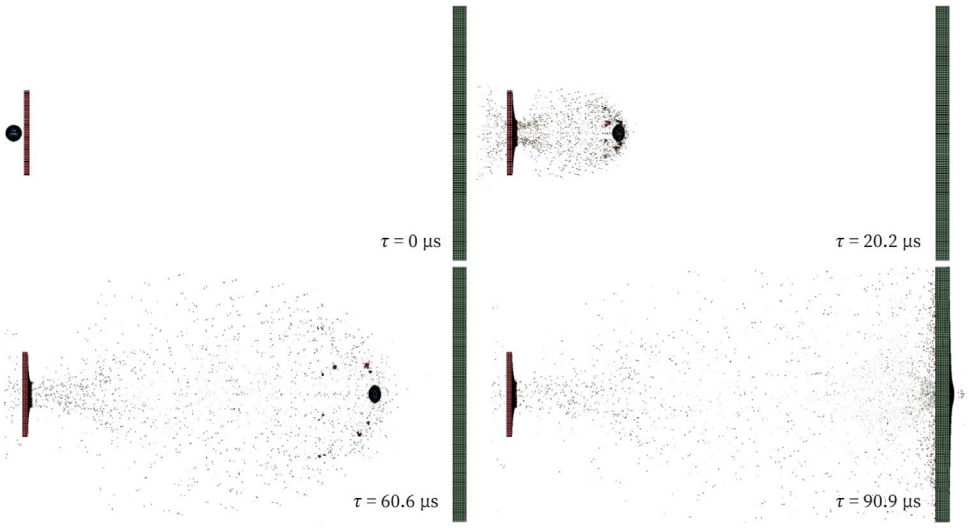

Fig. 16. Dual-wall Whipple shield (1.2 mm + 3.2 mm) impacted at 2 km/s by projectile with 3.8 mm diameter.

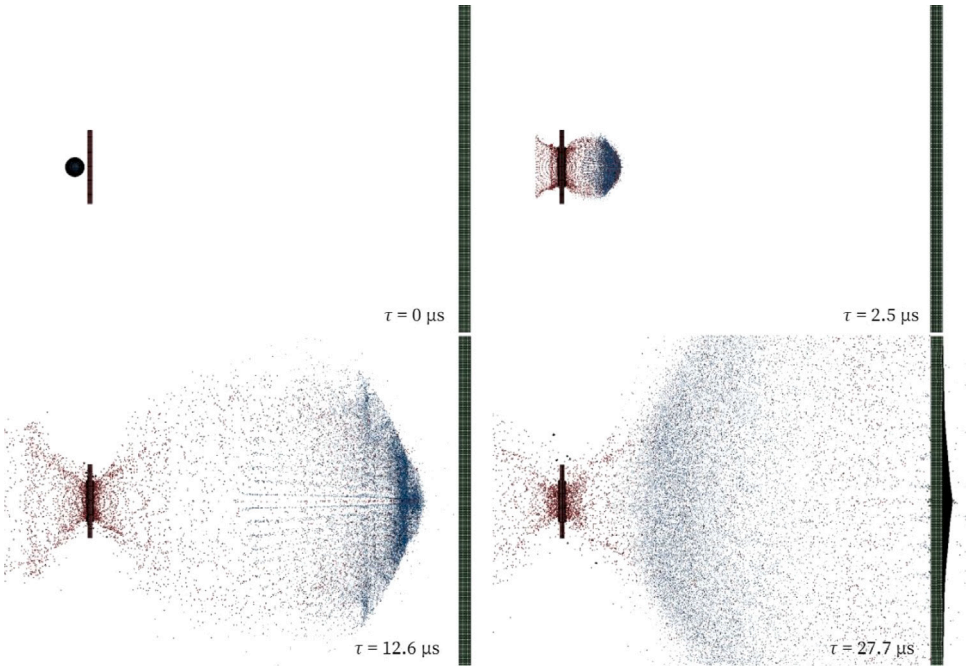

Fig. 17. Dual-wall Whipple shield (1.2 mm + 3.2 mm) impacted at 8 km/s by projectile with 5.2 mm diameter.

7. Concluding remarks

HVIs were modelled in LS-DYNA using a coupled finite element-discrete particle method (FEM/DEM), and the results were compared to experimental data from literature for validation. Impacts from orbital debris projectiles with diameters below 1 cm were considered, and AA6061-T6 was assumed for both the target and the projectile material. The numerical results showed that the FEM/DEM method can reproduce the experimental debris clouds from the literature and that the results with a linear EOS were in general closer to the experimental data than those with a non-linear Mie–Grüneisen EOS. The FEM/DEM method was applied to a dual-wall Whipple shield configuration and was able to accurately capture the damage from the debris cloud on the rear wall. The results obtained with the FEM/DEM method in this study are promising, and the method should be validated and compared to a larger set of experimental impact data, particularly experimental data with Whipple shields and other target materials.

Declaration of competing interest

The authors declare that they have no known competing financial interests or personal relationships that could have appeared to influence the work reported in this paper.

Acknowledgements

The present work has been carried out with financial support from the Centre of Advanced Structural Analysis (CASA), Centre for Research-based Innovation, at the Norwegian University of Science and Technology (NTNU) and the Research Council of Norway through project no. 237885 (CASA).

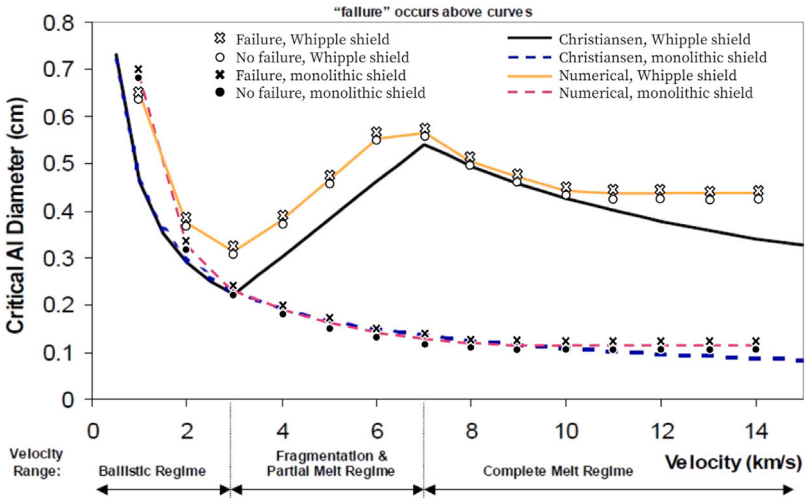

Fig. 18. Ballistic limit curves for monolithic and Whipple shields predicted with the FEM/DEM method and a linear EOS compared to the empirical curves by Christiansen [31]. The empirical curves are based on experimental test data for velocities up to 7 km/s, and extrapolated for velocities above 7 km/s.

References

[1] F.L. Whipple, Meteorites and space travel, Astron. J. 52 (1947) 131.

[2] E.L. Christiansen, K. Nagy, D.M. Lear, T.G. Prior, Space station MMOD shielding, Acta Astronaut. 65 (7–8) (2009) 921–929, http://dx.doi.org/10.1016/j.actaastro.2008.01.046.

[3] M.V. Silnikov, I.V. Guk, A.F. Nechunaev, N.N. Smirnov, Numerical simulation of hypervelocity impact problem for spacecraft shielding elements, Acta Astronaut. 150 (August 2017) (2018) 56–62, http://dx.doi.org/10.1016/j.actaastro.2017.08.030.

[4] S. Ren, Q. Zhang, Q. Wu, R. Long, L. Gong, Y. Lu, A reactive material double-bumper shield for centimeter sized projectile, Int. J. Impact Eng. 158 (April) (2021) 104028, http://dx.doi.org/10.1016/j.ijimpeng.2021.104028.

[5] Z. Xiaotian, J. Guanghui, H. Hai, Fragment identification and statistics method of hypervelocity impact SPH simulation, Chin. J. Aeronaut. 24 (1) (2011) 18–24, http://dx.doi.org/10.1016/S1000-9361(11)60003-4.

[6] C. Zhang, X. Chen, Y. Yuan, Characterization of the non-ideal debris cloud in yaw hypervelocity impact by cylindrical projectile, Int. J. Impact Eng. 155 (May) (2021) 103908, http://dx.doi.org/10.1016/j.ijimpeng.2021.103908.

[7] M.B. Liu, G.R. Liu, Smoothed particle hydrodynamics (SPH): An overview and recent developments, Arch. Comput. Methods Eng. 17 (2010) 25–76, http://dx.doi.org/10.1007/s11831-010-9040-7.

[8] E. Watson, M.O. Steinhauser, Discrete particle method for simulating hypervelocity impact phenomena, Materials 10 (4) (2017) 1–22, http://dx.doi.org/10.3390/ma10040379.

[9] E.P. Fahrenthold, B.A. Horban, A hybrid particle-finite element method for hypervelocity impact simulation, Int. J. Impact Eng. 23 (1 PART I) (1999) 237–248, http://dx.doi.org/10.1016/s0734-743x(99)00076-7.

[10] E.P. Fahrenthold, B.A. Horban, An improved hybrid particle-element method for hypervelocity impact simulation, Int. J. Impact Eng. 26 (1–10) (2001) 169–178, http://dx.doi.org/10.1016/s0734-743x(01)00079-3.

[11] G.R. Johnson, Linking of Lagrangian particle methods to standard finite element methods for high velocity impact computations, Nucl. Eng. Des. 150 (2–3) (1994) 265–274, http://dx.doi.org/10.1016/0029-5493(94)90143-0.

[12] G.R. Johnson, R.A. Stryk, Conversion of 3D distorted elements into meshless particles during dynamic deformation, Int. J. Impact Eng. 28 (9) (2003) 947–966, http://dx.doi.org/10.1016/S0734-743X(03)00012-5.

[13] G.R. Johnson, S.R. Beissel, C.A. Gerlach, Another approach to a hybrid particle-finite element algorithm for high-velocity impact, Int. J. Impact Eng. 38 (5) (2011) 397–405, http://dx.doi.org/10.1016/j.ijimpeng.2011.01.002.

[14] G.R. Johnson, S.R. Beissel, C.A. Gerlach, A combined particle-element method for high-velocity impact computations, Procedia Eng. 58 (2013) 269–278, http://dx.doi.org/10.1016/j.proeng.2013.05.031.

[15] X.T. Zhang, G.H. Jia, H. Huang, Finite element reconstruction approach for on-orbit spacecraft breakup dynamics simulation and fragment analysis, Adv. Space Res. 51 (3) (2013) 423–433, http://dx.doi.org/10.1016/j.asr.2012.09.023.

[16] Q.G. He, X. Chen, J.F. Chen, Finite element-smoothed particle hydrodynamics adaptive method in simulating debris cloud, Acta Astronaut. 175 (May) (2020) 99–117, http://dx.doi.org/10.1016/j.actaastro.2020.05.056.

[17] T. Børvik, S. Dey, L. Olovsson, M. Langseth, Impact of APM2 bullets on AA6082-T4 aluminium plates, in: F. Schäfer, S. Hiermaier (Eds.), Proceedings of the 11th Hypervelocity Impact Symposium, Freiburg, Germany, 2010, p. 13.

[18] A.J. Piekutowski, Formation and description of debris clouds produced by hypervelocity impact, in: NASA Contractor Report, University of Dayton Research Institute, 1996.

[19] G.R. Johnson, W.H. Cook, A constitutive model and data for metals subjected to large strains, high strain rates and high temperatures, in: Proceedings of the 7th International Symposium on Ballistics, 1983, pp. 541–547.

[20] D.J. Steinberg, S.G. Cochran, M.W. Guinan, A constitutive model for metals applicable at high-strain rate, J. Appl. Phys. 51 (3) (1980) 1498–1504, http://dx.doi.org/10.1063/1.327799.

[21] T. Børvik, O.S. Hopperstad, T. Berstad, M. Langseth, A computational model of viscoplasticity and ductile damage for impact and penetration, Eur. J. Mech. A Solids 20 (5) (2001) 685–712, http://dx.doi.org/10.1016/S0997-7538(01)01157-3.

[22] Y. Horie, Shock Wave Science and Technology Reference Library, Volume 2, Solids I, Springer, 2007.

[23] Livermore Software Technology (LST), LS-Dyna Theory Manual, Livermore Software Technology Corporation (LSTC), 2019.

[24] M.G. Cockroft, D.J. Latham, Ductility and workability of metals, J. Inst. Met. 96 (1968) 33–39.

[25] B.H. Frodal, K.O. Pedersen, T. Børvik, O.S. Hopperstad, Influence of pre-compression on the ductility of AA6xxx aluminium alloys, Int. J. Fract. 206 (2) (2017) 131–149, http://dx.doi.org/10.1007/s10704-017-0204-4.

[26] H.N. Wadley, T. Børvik, L. Olovsson, J.J. Wetzel, K.P. Dharmasena, O.S. Hopperstad, V.S. Deshpande, J.W. Hutchinson, Deformation and fracture of impulsively loaded sandwich panels, J. Mech. Phys. Solids 61 (2) (2013) 674–699, http://dx.doi.org/10.1016/j.jmps.2012.07.007.

[27] H. Granum, D. Morin, T. Børvik, O.S. Hopperstad, Calibration of the modified Mohr-Coulomb fracture model by use of localization analyses for three tempers of an AA6016 aluminium alloy, Int. J. Mech. Sci. 192 (October 2020) (2021) 106122, http://dx.doi.org/10.1016/j.ijmecsci.2020.106122.

[28] D. Steinberg, Equation of State and Strength Properties of Selected Materials, Lawrence Livwermore National Laboratory, Livermore, CA, United States, 1996, UCRL-MA-10.

[29] Livermore Software Technology (LST), LS-DYNA, 2021, https://www.lstc.com/products/ls-dyna. (Accessed 30 May 2021).

[30] Livermore Software Technology (LST), LS-DYNA R12 Keyword User's Manual. Vol. I, Livermore Software Technology Corporation (LSTC), 2020.

[31] E.L. Christiansen, Handbook for Designing MMOD Protection, Tech. rep., NASA, NASA Johnson Space Center, Astromaterials Research and Exploration Science Directorate, Human Exploration Science Office, 2009.